EUROPEAN ORGANIZATION FOR NUCLEAR RESEARCH

CERN-EP/89-98
14 August 1989

HIGH-p_T γ AND π^0 PRODUCTION, INCLUSIVE AND WITH A RECOIL HADRONIC JET, IN pp COLLISIONS AT $\sqrt{s}$ = 63 GeV

(The Axial Field Spectrometer Collaboration)

T. Åkesson[5], M.G. Albrow[15], S. Almehed[8], E. Anassontzis[1], R. Batley[5], O. Benary[16], H. Bøggild[6], O. Botner[6], H. Breuker[5], V. Burkert[2], B. Callen[12], R. Carosi[5], A.A. Carter[14], J.R. Carter[4], P.C. Cecil[4], V. Chernyatin[10], Y. Choi[13], W.E. Cleland[13], S. Dagan[16], E. Dahl-Jensen[6], I. Dahl-Jensen[6], P. Dam[6], G. Damgaard[6], B. Dolgoshein[10], S. Eidelman[11], M.W. Evans[15], C.W. Fabjan[5], I. Gavrilenko[9], U. Goerlach[5], Y. Goloubkov[10], H. Gordon[3], K.H. Hansen[6], V. Hedberg[9], J.W. Hiddleston[15], P. Ioannou[1], G. Jarlskog[9], T. Jensen[5], V. Kantserov[10], S. Katsanevas[5], C. Kourkoumelis[1], R. Kroeger[13], K. Kulka[9], D. Lissauer[16], B. Lörstad[9], I. Mannelli[5], A. Markou[1], N.A. McCubbin[15], U. Mjörnmark[9], R. Møller[6], W. Molzon[12], P. Nevsky[10], B.S. Nielsen[5], L.H. Olsen[5], Y. Oren[16], G. Piskounov[11], D.C. Rahm[3], L.K. Resvanis[1], A. Rudge[5], J. Schukraft[5], A. Shmeleva[8], V. Sidorov[11], S. Smirnov[10], H. Specht[7], N. Starinsky[10], I. Stumer[3], M. Sullivan[13], H.H. Thodberg[6], J.A. Thompson[13], G. Thorstenson[9], A. Vanyashin[10], E. Vella[12], J. Williamson[15], W.J. Willis[5], M. Winik[3], C. Woody[3] and A. Zhilin[10]

ABSTRACT

Direct photon and neutral pion production, inclusive and accompanying a hadronic jet, has been measured in pp collisions at the CERN Intersecting Storage Rings (ISR) for $\sqrt{s}$ = 63 GeV in the range $4.5 < p_T < 10$ GeV/c for the central pseudorapidity region $\eta \simeq 0$. Under the assumption that these events arise predominantly from the QCD Compton process, the gluon structure function in the range $0.15 < x < 0.30$ is calculated.

(Submitted to Yadernaya Fizika)

1) University of Athens, Athens, Greece.
2) Physikalisches Institut, University of Bonn, Fed. Rep. Germany.
3) Brookhaven National Laboratory, Upton, NY, USA.
4) University of Cambridge, UK.
5) CERN, Geneva, Switzerland.
6) Niels Bohr Institute, University of Copenhagen, Denmark.
7) Physikalisches Institut, University of Heidelberg, Fed. Rep. Germany.
8) P.N. Lebedev Institute of Physics, Moscow, USSR.
9) University of Lund, Sweden.
10) Moscow Physical Engineering Institute, Moscow, USSR.
11) Institute of Nuclear Physics, Novosibirsk, USSR.
12) University of Pennsylvania, Philadelphia, Pa., USA.
13) University of Pittsburgh, Pa., USA.
14) Queen Mary College, London, UK.
15) Rutherford Appleton Laboratory, Didcot, UK.
16) University of Tel Aviv, Israel.

1. INTRODUCTION

Since the discovery of direct photon production in pp collisions at the ISR [1–3] there has been increasing interest in the study of this process. Direct photons are clean probes of the gluon distribution inside protons via the QCD Compton effect [4–8].

In our previous paper [9] we calculated the gluon distribution on the basis of our photon–jet correlation data and the direct photon inclusive cross-section measured by the R806 experiment at CERN [2]. Since our previous publication, we have done a new, careful Monte Carlo study of our apparatus. The present accuracy of the energy-scale calibration reduces the systematic error of the direct photon inclusive spectrum measured in our experiment. In this paper we present the direct photon and neutral pion yield measured at the CERN Intersecting Storage Rings (ISR) for centre-of-mass energy $\sqrt{s} = 63$ GeV and transverse momenta between 4.5 and 10 GeV/c. The direct photon yield has been measured, as well as that of π^0's, detected in the same apparatus and under the same conditions. The results are compared with measurements at the same energy at $\eta \simeq 0$ [2, 3].

Based on this study, the photon–jet cross-section, with absolute normalization, is obtained and the gluon distribution function in the proton is calculated.

2. APPARATUS

The experiment was performed with the Axial Field Spectrometer (AFS) [10, 11]. Figure 1 shows the arrangement of the detectors at the ISR. The interaction region was surrounded by an inner hodoscope, consisting of 44 scintillation counters (not shown), a cylindrical drift chamber (DC), and a 2π uranium/copper/scintillator calorimeter (UCAL). For the detection of photons, the AFS was equipped with two high-granularity sodium iodide (NaI) walls, each covering a solid angle of 0.6 sr, centred at 90° in polar angle. A magnetic field of 5 kG, parallel to the direction of the colliding beams, allowed a measurement of the charged-particle momenta.

The drift chamber was subdivided azimuthally into 82 sectors of 4°, each containing 42 layers of sense wires. The DC angular acceptance was 2π (excluding two 16° wedges used for mechanical support) in azimuth and ± 1.0 in rapidity. Track coordinates were measured in the transverse x–y plane by drift time, with a spatial resolution of 230 μm, and by charge division in the z (beam) direction, giving a resolution of 1.5 cm. The resulting momentum error is 2% for a 1 GeV/c particle. Reconstructed tracks were required to satisfy the criteria listed below:

i) length of track > 25 cm;
ii) first digitizing within 32 cm from the intersection region;
iii) χ^2/number of degrees of freedom < 10;
iv) track to point at the common event vertex;
v) pseudorapidity of track $|\eta| \leq 0.9$.

The calorimeter, consisting of a 6 radiation lengths (X_0) electromagnetic part and a 3.6 absorption lengths (λ) hadronic part, surrounded the drift chamber, matching its angular acceptance. A high granularity was provided by subdividing into towers of 20×20 cm^2. The readout was done through wavelength shifters on two sides of the towers, for the electromagnetic and hadronic sections separately. In test measurements an energy resolution of $\sigma(E)/E = 16\%/\sqrt{E}$ was obtained for electromagnetic (e.m.) showers and $37\%/\sqrt{E}$ for hadronic showers.

The photon detectors (NaI 1 and NaI 2: one opposite and one in the direction of the c.m. motion) consisted of optically separated NaI crystals arranged in two walls of 20×30 elements at a distance of 107 cm from the interaction region [12]. The front faces of the crystals were 3.5×3.5 cm^2, and their length (13.8 cm) corresponded to $5.3X_0$. The total photon energy was measured by combining the energy deposition in the NaI and in the two UCAL sections behind it.

3. TRIGGER

The trigger system made use of the high granularity of the photon detectors by demanding (in coincidence with the event strobe defined by scintillators surrounding the beam pipe) a localized energy cluster in the NaI and in the electromagnetic part of UCAL behind the NaI. The thresholds used for the calorimeters away from the c.m. motion were 1.7 GeV in NaI1 and 1.0 GeV in the corresponding $UCAL_{em}$ wall. The thresholds for the calorimeters towards the c.m. motion were 2.0 GeV (NaI2) and 1.4 GeV ($UCAL_{em}$). Since more than one cluster was allowed, high-p_T π^0's and η's also triggered the system. The combined trigger threshold corresponds to approximately 4 GeV. The trigger was an OR between NaI1 and NaI2. A description of the various on- and off-line calibration systems can be found in Refs. [11] and [12].

The data were obtained from proton–proton collisions at $\sqrt{s} = 63$ GeV during 25 ISR runs in 1983. The integrated luminosity was

$$\int L\,dt = 1.6 \times 10^{37}\,cm^{-2}\,.$$

The recorded data used in the analysis consist of 918,802 events.

4. PRODUCTION OF HIGH-p_T γ's AND π^0's

4.1 Event selection

In the off-line analysis, only events that passed a software energy threshold (Table 1) were processed through the standard AFS program chain. This includes pattern recognition in the NaI detectors and in UCAL, and tracking plus vertex reconstruction for charged particles in the drift chamber. In order to reduce background from cosmic rays and beam–gas interactions, events were rejected if no vertex from charged particles was found in the beam-crossing region. The timing of the inner hodoscope and the beam–beam counters was required to be consistent with a single interaction allowing no second interaction within 30 ns of the nominal event time. Additional filtering was done by demanding that an event must contain an isolated e.m. shower with no further shower above 130 MeV in the same NaI wall (a direct photon candidate), or a good π^0 candidate with the energy of each individual shower being above 250 MeV.

The data sample for further analysis contained 136,540 events. The full data analysis was done separately for each of the NaI–UCAL detectors. The π^0's were identified as resolved pairs of photon showers.

For the calculation of the γ/π^0 ratio, the π^0's had to satisfy the following requirements:

i) both showers had to have an energy above 250 MeV;
ii) showers with a track pointing towards them were not combined with others to form π^0 candidates;
iii) no third shower above 180 MeV was tolerated in the event unless it was a charged particle as indicated by a track;
iv) the two-photon mass had to be within $80 \leq m_{\gamma\gamma} \leq 190$ MeV/c^2;
v) in order to decrease trigger-threshold uncertainties, a p_T cut of 4.5 GeV/c was applied.

The total selected π^0 statistics are 16,065 events in the NaI1 and 28,628 events in the NaI2. In Figs. 2a,b we show a typical $\gamma\gamma$ invariant mass spectrum for events from the 1983 pp run that passed all selection criteria. The experimental mass resolution varies from 20 to 50 MeV/c^2 for 4.5 to 10 GeV/c, respectively. The remaining background under the π^0 peak (2–4% depending on the p_T bin) was interpolated between the left and right levels of the background and subtracted.

The selection criteria for single photons were as follows:

i) no track was allowed to point at the single photon candidate;

ii) no second shower above 180 MeV was tolerated in the same NaI wall unless it was a charged particle as indicated by a track;

iii) the shower radius was required to be greater than 8 mm and less than 25 mm; this cut has been optimized by Monte Carlo methods and by looking at the radius of showers originating from clean π^0's;

iv) to decrease trigger-threshold uncertainties, a p_T cut of 4.5 GeV/c had to be made.

After these selection criteria were applied, the total direct-photon candidate sample contained 6,958 events in the NaI1 and 10,716 events in the NaI2.

The raw γ/π^0 ratio as a function of p_T is shown in Figs. 3a,b at $\sqrt{s}$ = 63 GeV. Also shown in these figures is the γ/π^0 background from meson decays. There are three contributions to this background:

i) meson decays where one shower fakes a direct photon candidate as the second shower falls outside the detector;

ii) asymmetric decays where one shower has a small energy and thus escapes the analysis cuts;

iii) merging of the two showers of a π^0 into one at high p_T because of the finite resolution of the detector.

The method of calculating this background has been described in detail in Ref. [13]. At high momenta the contribution of merging π^0's dominates the γ/π^0 background.

4.2 Correction for the reconstruction efficiencies and selection criteria

The effects of the trigger threshold, of the shower reconstruction algorithm, and of the cuts applied in the data analysis, have been studied by Monte Carlo methods. With the electromagnetic gamma-shower (EGS) code [14], which describes the development of e.m. showers, 21,803 events (7,803 γ's and 14,000 π^0's) have been generated at suitably chosen discrete momenta between 0.5 and 12 GeV/c. A careful study was carried out to ensure that the showers generated by EGS reproduce the characteristics of real showers measured at the ISR.

As an improvement to the method described in our previous paper [9], the calibration of EGS events was adjusted in such a way that the front-to-back ratio $E(NaI)/E(UCAL_{em})$ and the reconstructed π^0 mass in the EGS events gave the same average value as the real data. The effects of the finite detector resolution, of the detection efficiencies, and of the steepness of the π^0 spectrum were taken into account by the Monte Carlo program. Figures 4a,b compare the reconstructed π^0 mass for the experimental data and for the EGS events after calibration.

We have found that the transverse distributions of the EGS showers are narrower than those of the ISR data. Since the π^0 detection efficiency at high p_T was affected by the lateral shape, a correction was made to the reconstruction threshold of the EGS showers [13]. The generated π^0's and γ's were then used as input to the standard pattern-recognition program. Figure 5 shows the combined geometrical acceptance and reconstruction efficiency for π^0's and γ's in each wall. The bands indicate the statistical and systematic errors from the Monte Carlo calculation. The method of calculating this efficiency has been described in detail elsewhere [13]. In a similar way, by using the EGS events, the quality of the energy reconstruction was studied. The uncertainty in the absolute energy scale introduced by this method was estimated to be less than 3%. Possible differences in the energy scale between γ's and π^0's turned out to be less than 1%.

4.3 Results on the γ/π^0 ratio and inclusive cross-section for single-γ and π^0 production

After subtraction of the background and correction for the relative efficiency and acceptance of single γ's and π^0's, we obtained the corrected γ/π^0 ratio for each wall (Fig. 6a). The average γ/π^0

ratio for both walls compared with data from Ref. [2] is shown in Fig. 6b. The errors plotted in Fig. 6 include the quadratic combination of the following factors:

i) an error of 7–20% in the γ/π^0 ratio due to the uncertainty in the background subtraction;

ii) a 7% error in the relative π^0-to-γ reconstruction efficiency, as a result of statistical and systematic uncertainties in the EGS Monte Carlo;

iii) an error of 7% in the raw γ/π^0 ratio due to possible differences in the energy scale between γ's and π^0's.

For the single-photon cross-section calculation, the background was subtracted and the photon yield was corrected for the total efficiency (Fig. 5). It was assumed that the photon cross-section is independent of η within the pseudorapidity bin used for the Monte Carlo generation: $|\eta| < 0.7$.

It is clear that our isolation cut rejects a fraction of events where a soft particle — from processes that are not due to the hard scattering — fell into our acceptance. In order to calculate the inclusive cross-section, this effect was corrected in the same way as in Ref. [2]. The ratio of the π^0 cross-section, with and without the isolation cut, gave a correction factor of 1.15 for NaI1 and 1.25 for NaI2. It has been argued [15] that a difference in the event structure (the γ is alone, whereas the π^0 appears as a particle inside a jet) might lead to a distortion when using this procedure. A difference in the same-side multiplicity can be demonstrated by selecting only high p_T (e.g. above 800 MeV/c) for the associated tracks (Fig. 7). The effect of the different event structure on the correction factors was found to be less than 5%.

The inclusive photon cross-section at 90° c.m. for each NaI wall is shown in Fig. 8a. The measured inclusive cross-section for both walls (Fig. 8b) is compared with experimental data from Refs. [2] and [3] and with calculations by Owens [16], with Set 1 of Ref. [17] for gluon distribution and $Q^2 = (1/2)p_T^2$. Numerical values for the resulting cross-section are given in Table 2. The total errors given in the table are the combined statistical and systematic errors. The effects of the systematic errors on the final cross-section are listed in Table 3.

Figure 9a shows the results for the π^0 inclusive cross-section for each NaI wall. The resulting inclusive cross-section for both walls is shown in Fig. 9b, compared with experimental results of Ref. [2] and the calculation of Owens [16]. Numerical values are given in Table 4 and systematic errors in Table 5.

5. PHOTON–JET CROSS-SECTION

5.1 Recoil-jet selection

The recoil jets from single-photon and pion triggers were identified using UCAL information processed through a pattern-recognition program that grouped neighbouring towers into clusters, with NaI energy added to UCAL energy. The definition of a hadronic jet in our p_T range is somewhat ambiguous particularly in the lower end of the p_T range. We made tests using different jet-finding algorithms. The procedure finally selected is the following:

i) The jet momentum vector was formed as the vector sum of all clusters satisfying the following cuts:
   - Only individual clusters with $\Delta\phi > 120$ with respect to the trigger were summed up. The cut in $\Delta\phi$ was motivated by the energy flow (Fig. 10).
   - To reduce uncertainties due to energy leaks at the edges of the UCAL walls, we used only clusters with the z coordinate (along the beam), $|z| < 1000$ mm.
   - Only high-energy clusters (with $p_T > 800$ MeV/c) were used. This cut reduces the systematic error in the Monte Carlo calculation of jet detection efficiency.

ii) To reject events where the recoil jet missed UCAL, a threshold on p_T(jet) is introduced. The transverse momentum of the jet was required to be

$$p_T^{jet} > 0.3 p_T^{trig} ,$$

where p_T^{trig} is the trigger energy. The linear dependence of this threshold on p_T^{trig} makes the jet selection efficiency less dependent on trigger energy than the constant cut used in our previous analysis.

iii) All jets were restricted to the central region

$$|\eta_{jet}| < 0.3 .$$

This cut was motivated by acceptance losses in the jet rapidity distribution (Fig. 11). This figure and Fig. 12 (the azimuthal jet distribution) also show how the acceptance losses are reproduced in our Monte Carlo calculation. The difference between the two walls is due to the c.m. motion.

After the above cuts, we found 4592 direct-photon candidates with a central recoil jet. Figure 13 presents the raw ratio of the found γ–jet events N(γ–jet) to the number of photon candidates N(γ) in the same p_T^{trig} bin.

5.2 Monte Carlo simulation of jet detection

A total of 15,000 γ–jet events with high-p_T photons falling into the NaI acceptance, generated by the Lund Monte Carlo PYTHIA [18], were used to calculate the efficiency of our jet detection algorithm. PYTHIA simulates the hard scattering of free point-like partons within colliding hadrons and produces final-state jets according to the Lund string model for fragmentation. For our purpose, only events of the gluon Compton process were generated. We used the Monte Carlo program with parameters $Q^2 = (4/3)p_T^2$, $\Lambda = 0.3$ GeV, $\langle k_t^2 \rangle^{1/2} = 1.0$ GeV/c, and structure functions taken from Ref. [19]. The minimum transverse momentum required on the parton level (QTMIN), was chosen to be 2 GeV in order to account properly for the effects of the intrinsic parton motion. These events were passed through a simulation of UCAL [11], taking into account the energy and coordinate resolution of UCAL and the NaI.

The comparison of the azimuthal distribution of jets with respect to the trigger in experimental data and in the MC simulation (Fig. 12) seems to indicate an adequate choice of simulation parameters, particularly $\langle k_T \rangle$.

After applying the same set of cuts as in the data analysis, the jet detection correction factor R_{jet} was calculated as the ratio of N(γ–jet) found by algorithm to N(γ–quark) generated in the quark pseudorapidity interval $|\eta| < 0.3$. The jet detection correction factor was found to be independent of the photon p_T (within 10% accuracy), and equals

$$R_{jet} = 0.87 \pm 0.09$$

for both walls.

To estimate the systematic error in R_{jet} we made tests using different jet-finding algorithms and different PYTHIA parameters ($\langle k_T^2 \rangle$, QTMIN, Q^2). We found that these uncertainties lead to the error in R_{jet}, which is about 10%.

5.3 The results on the double inclusive photon–jet cross-section

To calculate the double inclusive photon–jet cross-section, we used the formula

$$d^3\sigma/d\eta_\gamma \, d\eta_{jet} \, dp_T = [N(\gamma\text{–jet})/N(\gamma)]/(\Delta\eta_{jet} \, R_{jet}) \times d^2\sigma/d\eta_\gamma \, dp_T ,$$

where N(γ–jet)/N(γ) is the photon–jet correlation ratio (Fig. 13) and R_{jet} is the jet-detection correction factor calculated above (see subsection 5.2). The cross-section $d^2\sigma/d\eta_\gamma dp_T$ was determined in Section 4.

The background contribution to the gamma–jet correlation from π^0's was studied by comparing the γ(candidate)–jet with the π^0–jet ratios. Figure 14 shows the ratio of the photon–jet correlation to the pion–jet correlation, consistent with unity within statistical errors. The same result was obtained (using another jet-finding algorithm) in our previous paper [9]. Thus, the gamma(candidate)–jet correlation shown in Fig. 13 reproduces the direct-gamma–jet correlation (within a systematic error of 5% due to the background). The results for the direct-gamma – away-side-jet cross-section are given in Table 6. Systematic errors are given in Table 7. Within systematic errors this final result agrees with our previous analysis [9] in which the R808 inclusive γ spectrum was used as a normalization.

Our measured photon–jet cross-section compared with the QCD theory is shown in Fig. 15. The QCD calculation was taken from Ref. [16] with the Set 1 gluon distribution from Ref. [17].

6. GLUON STRUCTURE FUNCTION

6.1 Determination of the gluon distribution

The photon–jet cross-section, when the photon and the recoil jet are detected close to 90°, is directly related to the quark and gluon densities [$F_2(x)$ and $G(x)$] multiplied by the QCD interaction cross-section at the parton level [4–8]:

$$\left(\frac{d^3\sigma}{d\eta_\gamma d\eta_{jet} dp_T}\right)_{\eta_\gamma = \eta_{jet} = 0} = K\frac{5}{3}\,\alpha\cdot\alpha_s\,\frac{1}{x^2}\,\frac{1}{s^{3/2}}\,G(x)F_2(x)\ ,$$

where $x = 2p_T/\sqrt{s}$.

This formula neglects all non-gluon Compton contributions to the cross-section. In a separate publication [13] we have shown, by a comparison of direct-photon production in pp and $p\bar{p}$ interactions, that contributions from the annihilation process are small in single-nucleon collisions. A calculation [20] estimates the contribution of the annihilation process to the total photon cross-section to be 8.7%. Contributions from bremsstrahlung processes were estimated to be $\leq$ 30% [16].

Several different approaches were made in order to describe the R806/R807 photon cross-section [11] within QCD. Owens [16] made an analytic leading order QCD calculation. Contogouris et al. [21] derive rules for determining a K-factor (first introduced to explain the discrepancy between QCD prediction of lepton-pair production through the Drell–Yan process and the experimental data) to account for higher-order processes. Both methods lead to a satisfactory agreement with the data.

The function $F_2(x)$ has been measured with high precision using neutrino and muon beams on isoscalar targets. For the calculation of $xG(x)$, we used $F_2(x)$, taken from the EMC [22].

For the strong coupling constant we used the expression $\alpha_s = 12\pi/[25\ \ln\ (Q^2/\Lambda^2)]$ in our calculation.

Owing to the weak sensitivity of the photon–jet cross-section on the QCD scale parameter Λ, the latter cannot be extracted from our data independently. We varied Λ in the range 0.15 to 0.25 GeV, with a resulting variation of $\pm$7% in our result. Our final choice was Λ = 0.2 GeV.

The influence of higher-order QCD processes must be included. The Contogouris approach [21] yields an effective correction factor $K \approx 1.7$ for Compton scattering. From estimates of the relative importance of bremsstrahlung and annihilation, the K-factor is increased to 2.7 for the inclusive γ–jet process.

The K-factor, $F_2(x,Q^2)$, and α_s are coupled with the Q^2 choice, which is ambiguous in hadronic interactions. We used three different scales, $Q^2 = p_T^2$ (as in Ref. 21), $Q^2 = (4/3)p_T^2$, and $Q^2 = 2p_T^2$, in order to estimate the dependence of our result. We find $\pm$5% differences due to the α_s and the

K-factor variations. The influence of $F_2(x,Q^2)$ dependence on this Q^2 choice is negligible as $dF_2(x,Q^2)/d \ln Q^2$ crosses zero inside our x region. The final calculation was done with $Q^2 = (4/3)p_T^2$.

Our result for xG(x) is given in Table 8 for the individual x bins and is presented in Fig. 16, where we also show statistical and systematic errors. The systematic errors are the quadratic combination of the errors given in Table 9.

6.2 Estimate of the Q^2 value in measured gluon distribution

The standard choice of the Q^2 variable is the same as that used in α_s and in structure functions. However, for structure functions, $Q^2 \approx p_T^2$ is not always the relevant one. According to the theoretical analysis of ref. [8], the variable Q^2 in parton distributions for the process $p + p \rightarrow \gamma +$ jet + anything is determined by the maximum allowed value of the photon–jet momentum imbalance $\Delta^2 = [p_T(\gamma) - p_T(\text{jet})]^2$. The value of Δ^2_{max} controls the amount of soft gluon radiation emitted by initial partons and thus determines the virtual parton distributions [23]. In inclusive γ production, when no away-side jet selection is performed, all values of Δ up to p_T are present. Therefore, in the inclusive γ cross-section analysis, $Q^2 \approx p_T^2$ is a relevant choice for use in structure functions. But in our experiment, the jet-selection procedure rejects events when soft gluon radiation carries away a significant part of the jet momentum. Estimates show that $\Delta^2_{max} = 5$–10 GeV^2 seems to be a proper value for the variable Q^2 in the gluon distribution measured by our experiment.

6.3 Comparison with other experiments

The gluon structure function calculated in our previous publication [9] agrees with this final analysis within systematic errors. The variations are mainly due to differences in inclusive photon spectra measured by R806 and this experiment (Fig. 8b).

In Fig. 16 the measured gluon structure function is compared with some recent results on the gluon distribution calculated from deep-inelastic scattering (DIS) data [22, 24, 25]. It should be noticed that in the analysis of DIS data, the QCD scale parameter Λ and the gluon distribution are strongly correlated and cannot be determined unambiguously. This analysis also depends on the order of QCD approximation used. The results obtained in a next-to-leading-order approximation ($\overline{MS}$) and with $\Lambda = 0.2$ GeV by the BCDMS Collaboration [25] agree better with our gluon distribution.

7. CONCLUSIONS

We have measured the invariant cross-section of single-photon and π^0 production in pp collisions for $\sqrt{s} = 63$ GeV in the range $4.5 < p_T < 10$ GeV/c along with the double inclusive cross-section of photon plus recoil-jet production.

Using these spectra, the gluon distribution function was measured. Our result is consistent with the BCDMS parametrization [25], obtained from deep-inelastic scattering data using a next-to-leading-order approximation.

Acknowledgements

We wish to thank the ISR Experimental Support and Operations Groups for providing excellent conditions throughout this experiment. We thank Yu. Nikitin, A. Kalinowsky and S. Ivanov, and A.P. Contogouris for stimulating discussions. Support from the Research Councils in our home countries is gratefully acknowledged.

REFERENCES

[1] M. Diakonou et al., Phys. Lett. **87B** (1979) 292 and **91B** (1980) 296.

[2] E. Anassontzis et al., Z. Phys. **C13** (1982) 277.

[3] A.L.S. Angelis et al., Phys. Lett. **94B** (1980) 106.

[4] H. Fritzsch and P. Minkowski, Phys. Lett. **69B** (1977) 316.

[5] F. Halzen, M. Dechantsreiter and D.M. Scott, Phys. Rev. **D22** (1980) 1617.

[6] L. Cormell and J.F. Owens, Phys. Rev. **D22** (1980) 1609.

[7] R. Baier, J. Engels and B. Petersson, Z. Phys. **C6** (1980) 309.
P. Aurenche et al., Phys. Lett. **169B** (1986) 441.

[8] A.V. Vanyashin, A.V. Zhilin and Yu.P. Nikitin, Sov. J. Nucl. Phys. **39** (1984) 608.

[9] T. Åkesson et al., Z. Phys. **C34** (1987) 293.

[10] O. Botner et al., Nucl. Instrum. Methods **179** (1981) 45 and **196** (1982) 314.
H. Gordon et al., Nucl. Instrum. Methods **196** (1982) 303.

[11] T. Åkesson et al., Nucl. Instrum. Methods **A241** (1985) 17.

[12] R. Batley et al., Nucl. Instrum. Methods **A242** (1985) 75.

[13] T. Åkesson et al., Phys. Lett. **158B** (1985) 282.

[14] R.L. Ford and W.R. Nelson, SLAC-210 (1978).

[15] T. Ferbel and W.R. Molzon, Rev. Mod. Phys. **57** (1984) No. 2.

[16] J.F. Owens, Rev. Mod. Phys. **59** (1987) No. 2.

[17] D.W. Duke and J.F. Owens, Phys. Rev. **D30** (1984) 49.

[18] H.U. Bengtsson and G. Ingelman, Comput. Phys. Commun. **34** (1985) 251.

[19] M. Glück, E. Hoffmann and E. Reya, Z. Phys. **C13** (1982) 119.

[20] E.L. Berger, E. Braaten and R.D. Field, Nucl. Phys. **B239** (1984) 52.

[21] A.P. Contogouris and H. Tanaka, Phys. Rev. **D33** (1986) 1265.
A.P. Contogouris, S. Papadopoulos and J. Ralston, Phys. Rev. **D25** (1982) 1280 and Phys. Lett. **104B** (1981) 70.

[22] J.J. Aubert et al., Nucl. Phys. **B259** (1985) 189 and **B272** (1986) 158.

[23] Yu.L. Dokshitzer, D.I. Dyakonov and S.I. Troyan, Phys. Rep. **58** (1980) 269.

[24] J.V. Allaby et al., Phys. Lett. **197B** (1987) 281.

[25] A.C. Benvenuti et al. (BCDMS Collab.), Statistical measurement of the proton structure function and test of QCD from deep inelastic muon scattering at high Q^2, paper No. 218 submitted to the Int. Symp. on Lepton and Photon Interactions at High Energies, Hamburg, 1987.

Table 1

Software energy thresholds (GeV)

	NaI 1	NaI 2
E_{tot} [a)]	3.1	3.9
E(NaI)	1.7	2.0
$E(UCAL_{em})$	1.0	1.4

a) Energy summed up as NaI + $UCAL_{em}$ + $UCAL_{had}$

Table 2

Invariant cross-section for the reaction $p + p \rightarrow \gamma +$ anything

p_T range (GeV/c)	$\langle p_T \rangle$ (GeV/c)	$E(d^3\sigma/dp^3)$ $(cm^2/GeV^2\,c^{-3})$
4.5– 5.0	4.75	$(3.14 \pm 0.79) \times 10^{-34}$
5.0– 5.5	5.25	$(1.22 \pm 0.27) \times 10^{-34}$
5.5– 6.0	5.73	$(5.96 \pm 1.22) \times 10^{-35}$
6.0– 6.5	6.23	$(3.20 \pm 0.63) \times 10^{-35}$
6.5– 7.0	6.74	$(1.87 \pm 0.35) \times 10^{-35}$
7.0– 7.5	7.23	$(9.07 \pm 1.82) \times 10^{-36}$
7.5– 8.0	7.72	$(6.20 \pm 1.26) \times 10^{-36}$
8.0– 8.5	8.22	$(3.81 \pm 0.86) \times 10^{-36}$
8.5– 9.0	8.74	$(2.54 \pm 0.63) \times 10^{-36}$
9.0–10.0	9.44	$(1.26 \pm 0.32) \times 10^{-36}$
10.0–11.0	10.36	$(6.05 \pm 1.92) \times 10^{-37}$

Table 3

Uncertainties in the absolute normalization of the inclusive photon cross-section (in %)

Background subtraction	±7–20
Reconstruction efficiency	±5–20
Uncertainty in the absolute energy scale (estimated change of the cross-section)	±18–25
Correction factors for the inclusive cross-section	±5
Luminosity	±10

Table 4

Invariant cross-section for the reaction $p + p \rightarrow \pi^0 + \text{anything}$

p_T range (GeV/c)	$\langle p_T \rangle$ (GeV/c)	$E(d^3\sigma/dp^3)$ ($cm^2/GeV^2\,c^{-3}$)
4.5– 5.0	4.75	$(2.61 \pm 0.68) \times 10^{-33}$
5.0– 5.5	5.25	$(9.45 \pm 2.35) \times 10^{-34}$
5.5– 6.0	5.73	$(4.00 \pm 0.90) \times 10^{-34}$
6.0– 6.5	6.23	$(2.00 \pm 0.46) \times 10^{-34}$
6.5– 7.0	6.73	$(1.01 \pm 0.23) \times 10^{-34}$
7.0– 7.5	7.23	$(5.50 \pm 1.25) \times 10^{-35}$
7.5– 8.0	7.72	$(2.59 \pm 0.59) \times 10^{-35}$
8.0– 8.5	8.23	$(1.37 \pm 0.31) \times 10^{-35}$
8.5– 9.0	8.75	$(7.32 \pm 1.98) \times 10^{-36}$
9.0–10.0	9.38	$(3.02 \pm 0.84) \times 10^{-36}$
10.0–11.0	10.40	$(6.70 \pm 2.64) \times 10^{-37}$

Table 5

Uncertainties in the absolute normalization of the π^0 inclusive cross-section (in %)

Background subtraction	±2
Reconstruction efficiency	±5–20
Uncertainty in the absolute energy scale (estimated change of the cross-section)	±21
Luminosity	±10

Table 6

Direct photon–jet cross-section

p_T (GeV/c)	γ–jet correlation $[(N_{\gamma\text{-jet}}/N_\gamma)/R_{jet}]$	$d^3\sigma/d\eta_\gamma\, d\eta_{jet}\, dp_T$ with statistical error (cm^2/GeV)	Total error
4.75	0.277 ± 0.007	$(4.31 \pm 0.17) \times 10^{-33}$	1.24×10^{-33}
5.24	0.275 ± 0.009	$(1.85 \pm 0.10) \times 10^{-33}$	0.46×10^{-33}
5.73	0.314 ± 0.013	$(1.12 \pm 0.07) \times 10^{-33}$	0.26×10^{-33}
6.23	0.327 ± 0.016	$(6.95 \pm 0.55) \times 10^{-34}$	1.57×10^{-34}
6.74	0.345 ± 0.020	$(4.53 \pm 0.45) \times 10^{-34}$	1.01×10^{-34}
7.23	0.331 ± 0.025	$(2.28 \pm 0.33) \times 10^{-34}$	0.57×10^{-34}
7.73	0.345 ± 0.031	$(1.74 \pm 0.29) \times 10^{-34}$	0.45×10^{-34}
8.22	0.339 ± 0.037	$(1.09 \pm 0.24) \times 10^{-34}$	0.31×10^{-34}
8.74	0.503 ± 0.054	$(1.25 \pm 0.28) \times 10^{-34}$	0.35×10^{-34}
9.42	0.383 ± 0.049	$(4.20 \pm 1.11) \times 10^{-35}$	1.33×10^{-35}
10.40	0.402 ± 0.077	$(3.09 \pm 1.02) \times 10^{-35}$	1.18×10^{-35}

Table 7

Systematic errors on $d^3\sigma/d\eta_\gamma\, d\eta_{jet}\, dp_T$ (in %)

Inclusive photon cross-section	(see Table 3)
Jet-finding correction factor calculation	10
Different algorithms on the jet selection	10
Background subtraction in N(γ–jet)/N(γ)	5

Table 8
Calculation of xG(x)

x	Q^2	α_s	F_2	xG	Total error
0.150	30.1	0.228	0.331	1.210 ± 0.047	0.360
0.167	36.7	0.221	0.326	0.736 ± 0.038	0.192
0.183	44.1	0.215	0.320	0.612 ± 0.039	0.152
0.198	52.1	0.210	0.314	0.509 ± 0.040	0.123
0.214	60.7	0.206	0.306	0.438 ± 0.043	0.105
0.230	70.1	0.202	0.297	0.285 ± 0.041	0.075
0.246	80.1	0.198	0.288	0.280 ± 0.047	0.077
0.262	90.7	0.195	0.278	0.223 ± 0.049	0.066
0.278	102	0.192	0.268	0.321 ± 0.073	0.094
0.302	120	0.188	0.252	0.150 ± 0.040	0.049
0.333	147	0.184	0.229	0.168 ± 0.056	0.066

Table 9
Systematic errors on xG(x) (in %)

Systematic errors on $d^3\sigma/d\eta_\gamma\, d\eta_{jet}\, dp_T$	(see Table 7)
Ambiguity in Q^2	5
Ambiguity in Λ	7

Figure captions

Fig. 1 Experimental set-up.

Fig. 2 Two-photon mass spectrum after analysis cuts: a) NaI 1, b) NaI 2.

Fig. 3 Observed ratio of γ/π^0 at $\sqrt{s} = 63$ GeV. The indicated band shows the result of the Monte Carlo calculation of the remaining background from π^0, η, η', and ω meson decays. The dashed line indicates the contribution of π^0's with both showers falling inside the NaI: a) NaI 1, b) NaI 2.

Fig. 4 Reconstructed π^0 mass after analysis cuts. The band shows the result of the Monte Carlo calculation: a) NaI 1, b) NaI 2.

Fig. 5 Combined geometrical acceptance and reconstruction efficiency for γ's and π^0's versus p_T. The bands indicate the total errors of the Monte Carlo calculation.

Fig. 6 The γ/π^0 corrected ratio:
a) separately for NaI 1 and NaI 2;
b) resulting ratio compared with the data from Exp. R806 [2].

Fig. 7 Angular distribution of charged particles in γ and π^0 events.

Fig. 8 Inclusive direct-photon cross-section as a function of p_T:
a) separately for NaI 1 and NaI 2;
b) resulting cross-section compared with R806 [2] and CCOR [3] data and with the calculation of Ref. [16].

Fig. 9 Inclusive π^0 cross-section as a function of p_T:
a) obtained for NaI 1 and NaI 2;
b) resulting cross-section compared with R806 [2] data and with the calculation of Ref. [16].

Fig. 10 Energy flow measured in UCAL in direct-photon events.

Fig. 11 Rapidity distribution of recoil jets for events with a direct photon in a) NaI 1, b) NaI 2. Dotted curve: the Monte Carlo calculation based on the Lund model.

Fig. 12 Azimuthal distribution in $\Delta\phi$ of recoil jets for events with a direct photon in a) NaI 1, b) NaI 2. Dotted curve: the Monte Carlo calculation based on the Lund model.

Fig. 13 Photon–jet correlation ratio.

Fig. 14 Ratio of photon–jet correlation to π^0–jet correlation.

Fig. 15 Double inclusive photon–jet cross-section and comparison with the QCD calculation [16].

Fig. 16 Results on gluon distribution and comparison with BCDMS [25], CHARM [24], and EMC [22] results, with leading-order (LO) and next-to-leading-order ($\overline{\text{MS}}$) corrections.

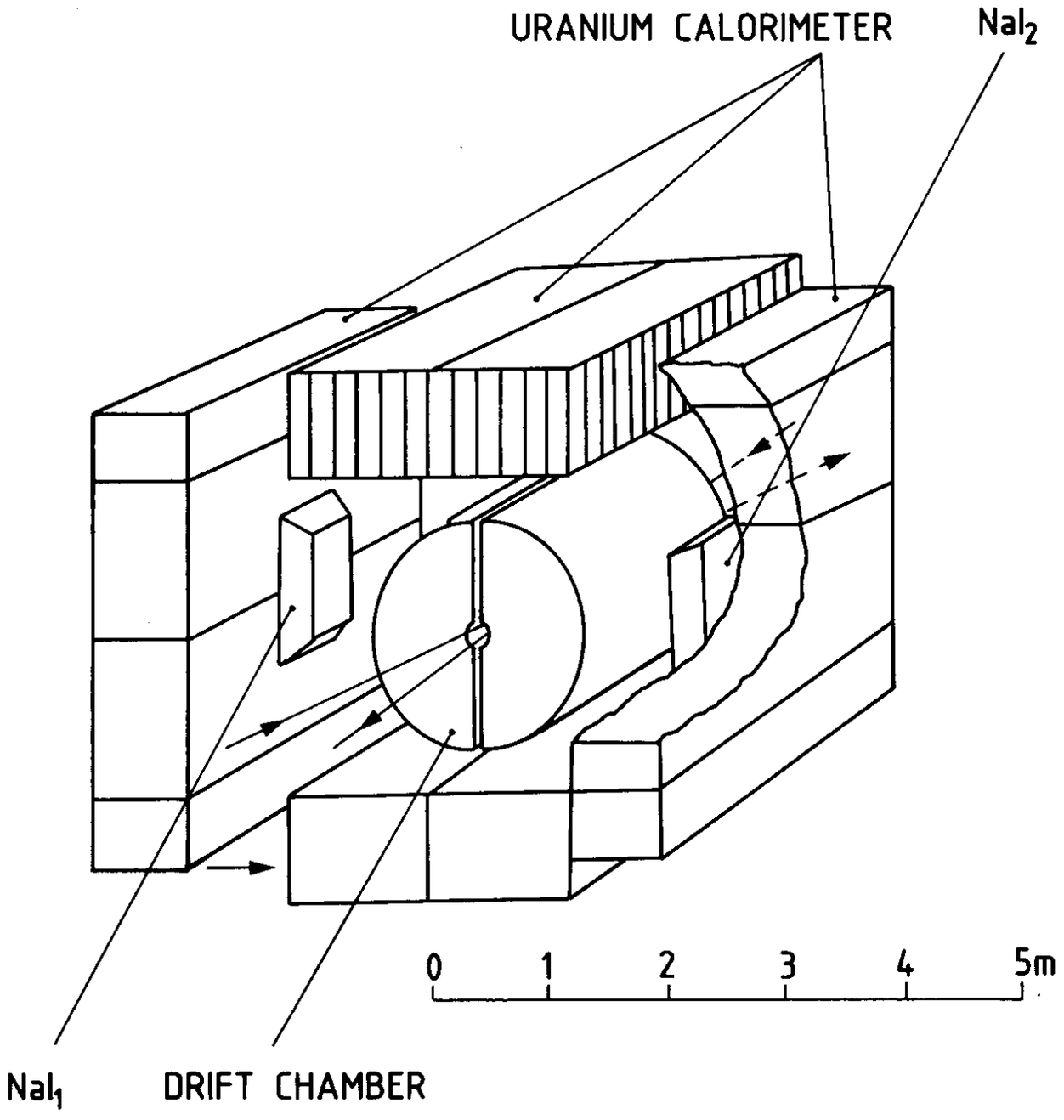

Fig. 1

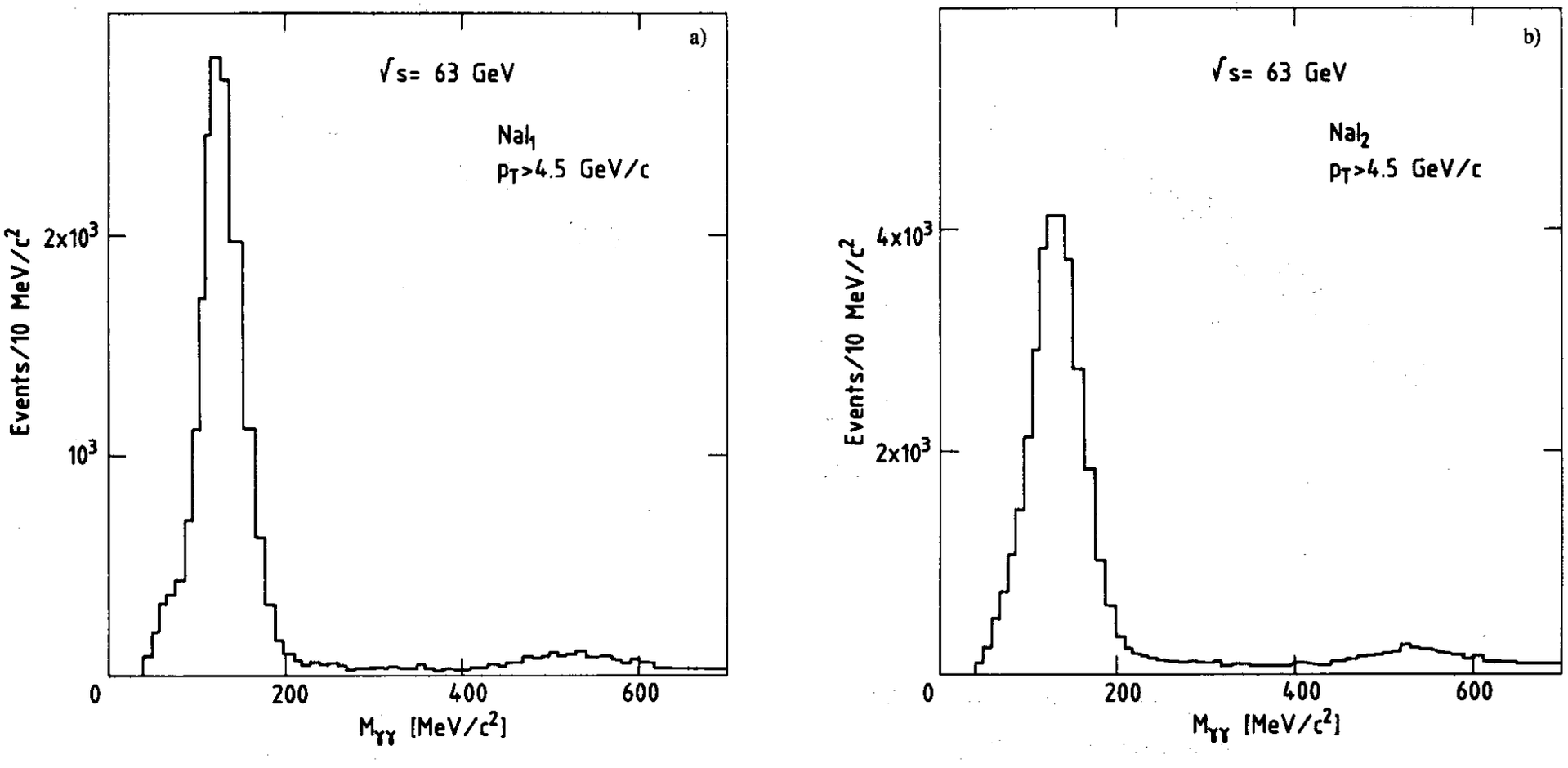
a)
√s= 63 GeV
NaI1
pT>4.5 GeV/c
Events/10 MeV/c2
2x10^3
10^3
0
200
400
600
Mγγ [MeV/c2]
b)
√s= 63 GeV
NaI2
pT>4.5 GeV/c
Events/10 MeV/c2
4x10^3
2x10^3
0
200
400
600
Mγγ [MeV/c2]

Fig. 2

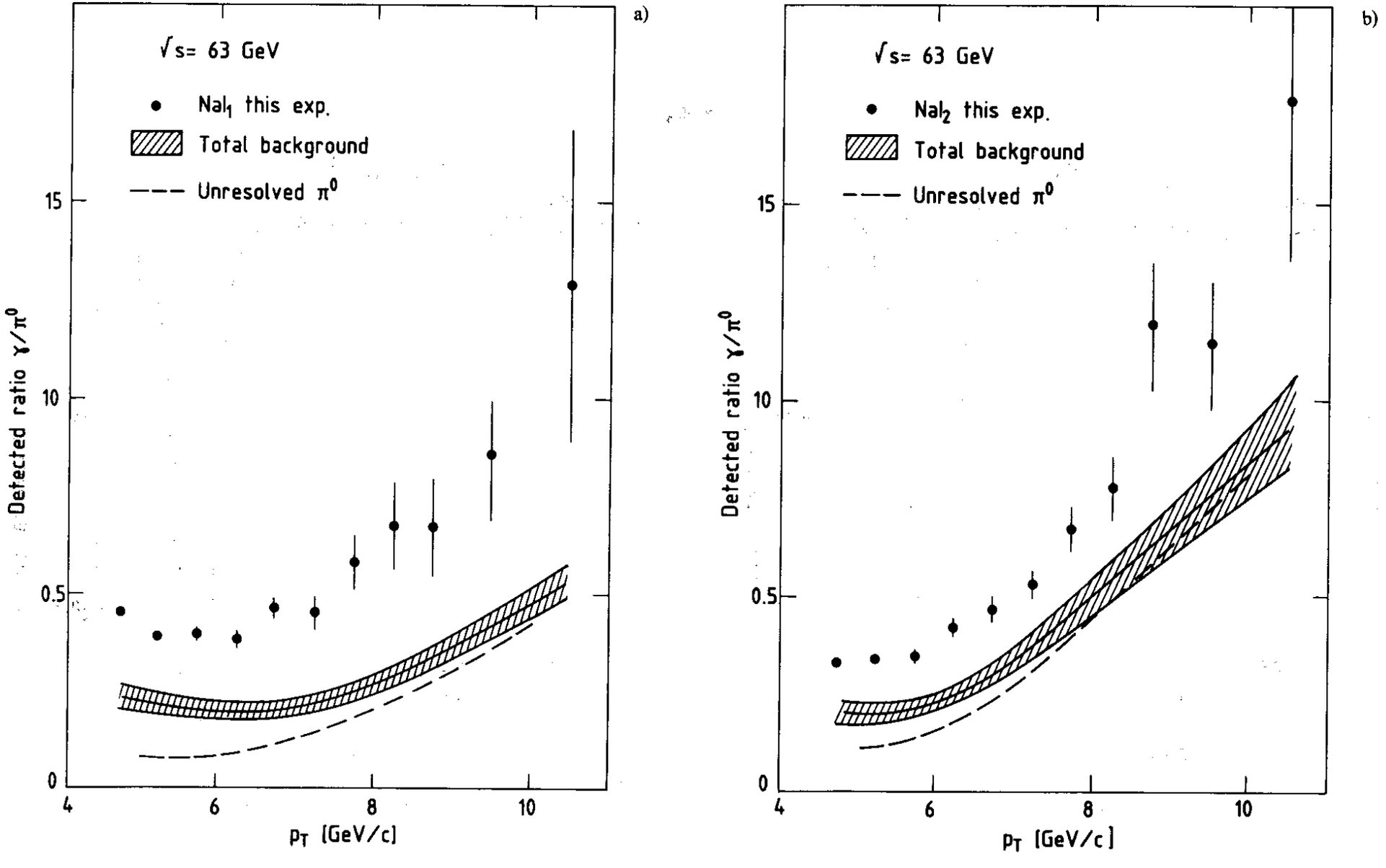
a)
√s= 63 GeV
NaI1 this exp.
Total background
Unresolved π0
Detected ratio γ/π0
pT [GeV/c]
b)
√s= 63 GeV
NaI2 this exp.
Total background
Unresolved π0
Detected ratio γ/π0
pT [GeV/c]

Fig. 3

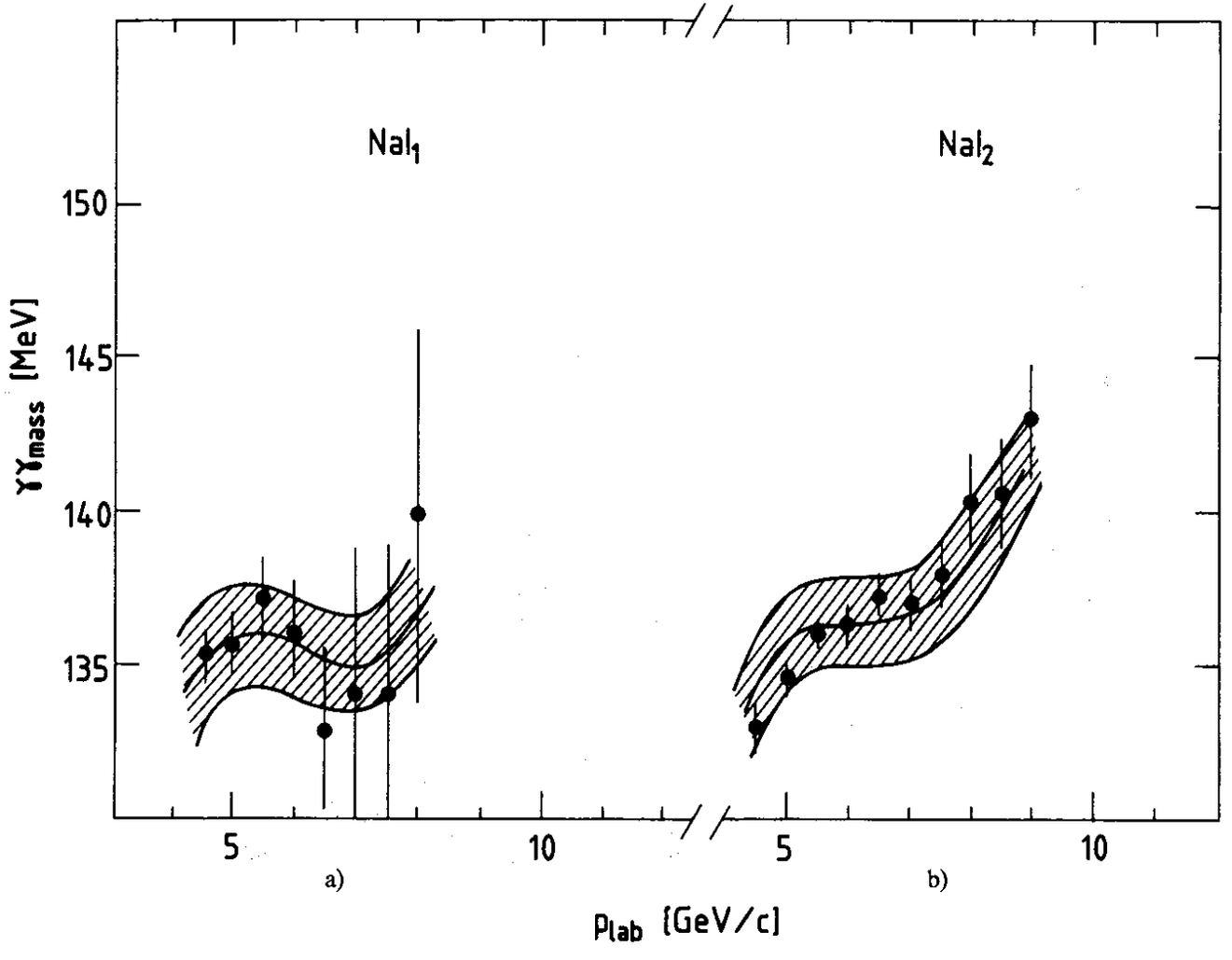

Fig. 4

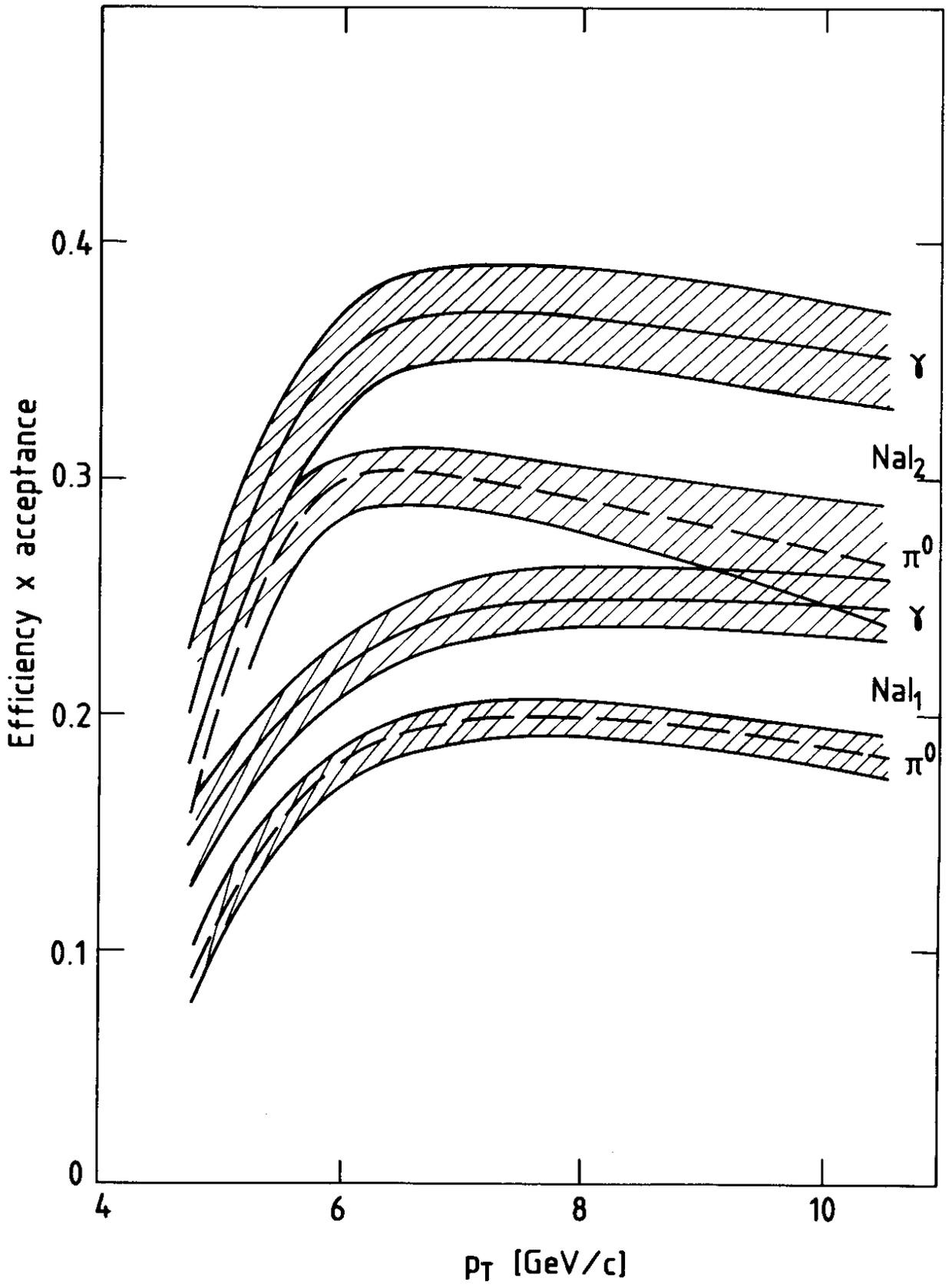
Efficiency x acceptance
0.4
0.3
0.2
0.1
0
4
6
8
10
p_T [GeV/c]
γ
NaI$_2$
π^0
γ
NaI$_1$
π^0

Fig. 5

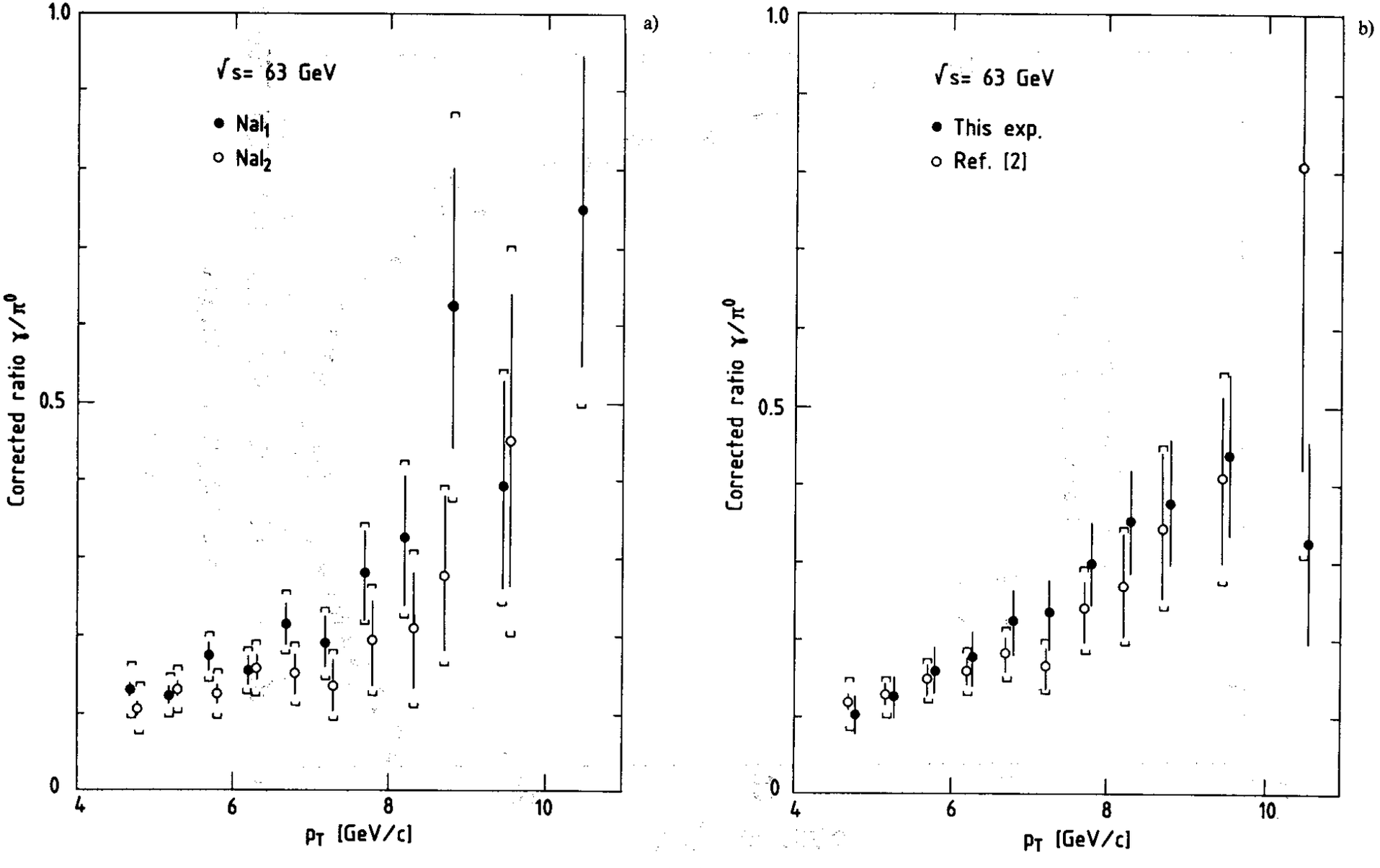
a)
√s= 63 GeV
● Nal1
○ Nal2
Corrected ratio γ/π0
pT [GeV/c]
b)
√s= 63 GeV
● This exp.
○ Ref. [2]
Corrected ratio γ/π0
pT [GeV/c]

Fig. 6

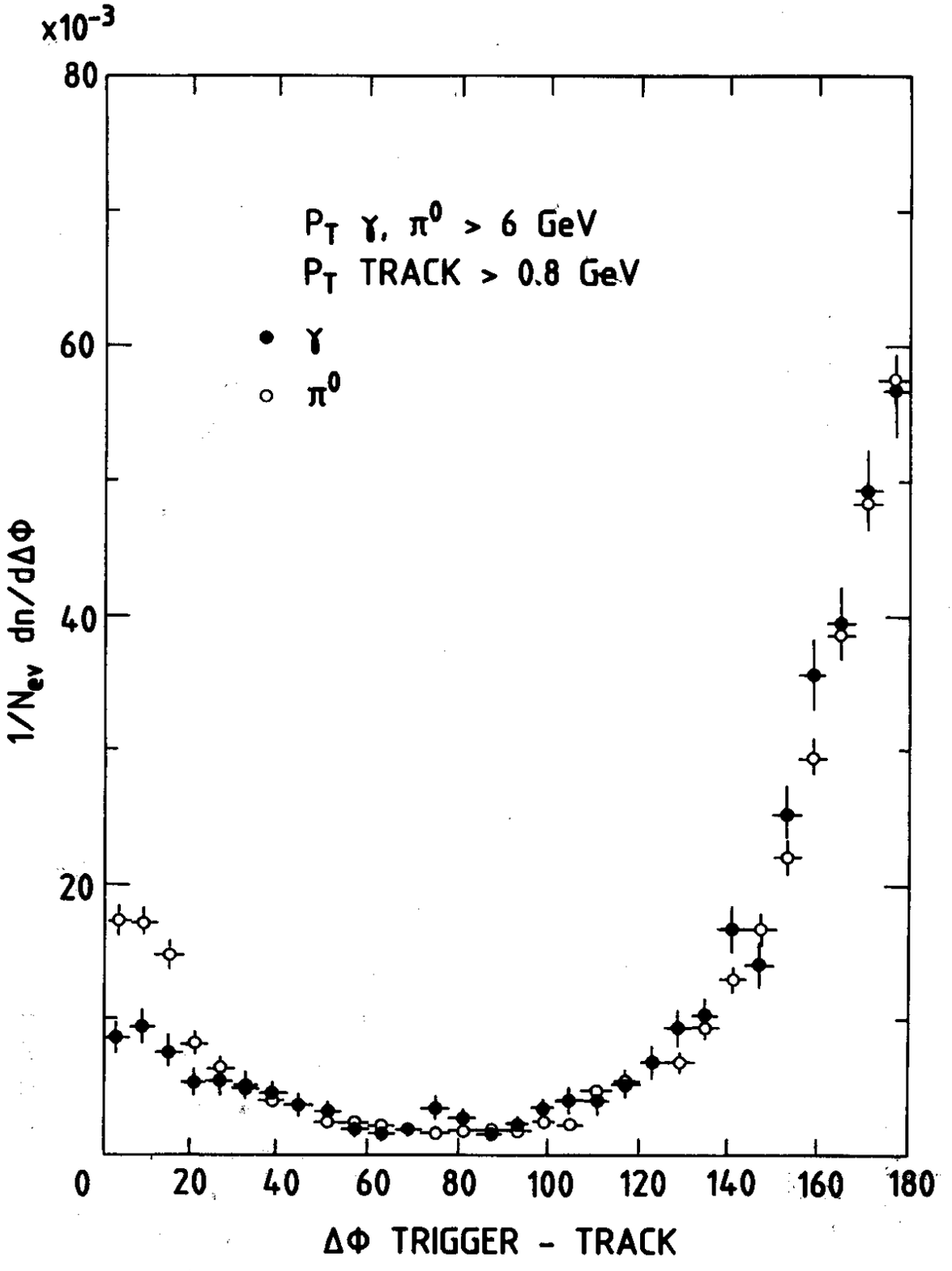
x10⁻³
80
60
40
20
0
20
40
60
80
100
120
140
160
180
P_T γ, π⁰ > 6 GeV
P_T TRACK > 0.8 GeV
γ
π⁰
1/N_ev dn/dΔΦ
ΔΦ TRIGGER - TRACK

Fig. 7

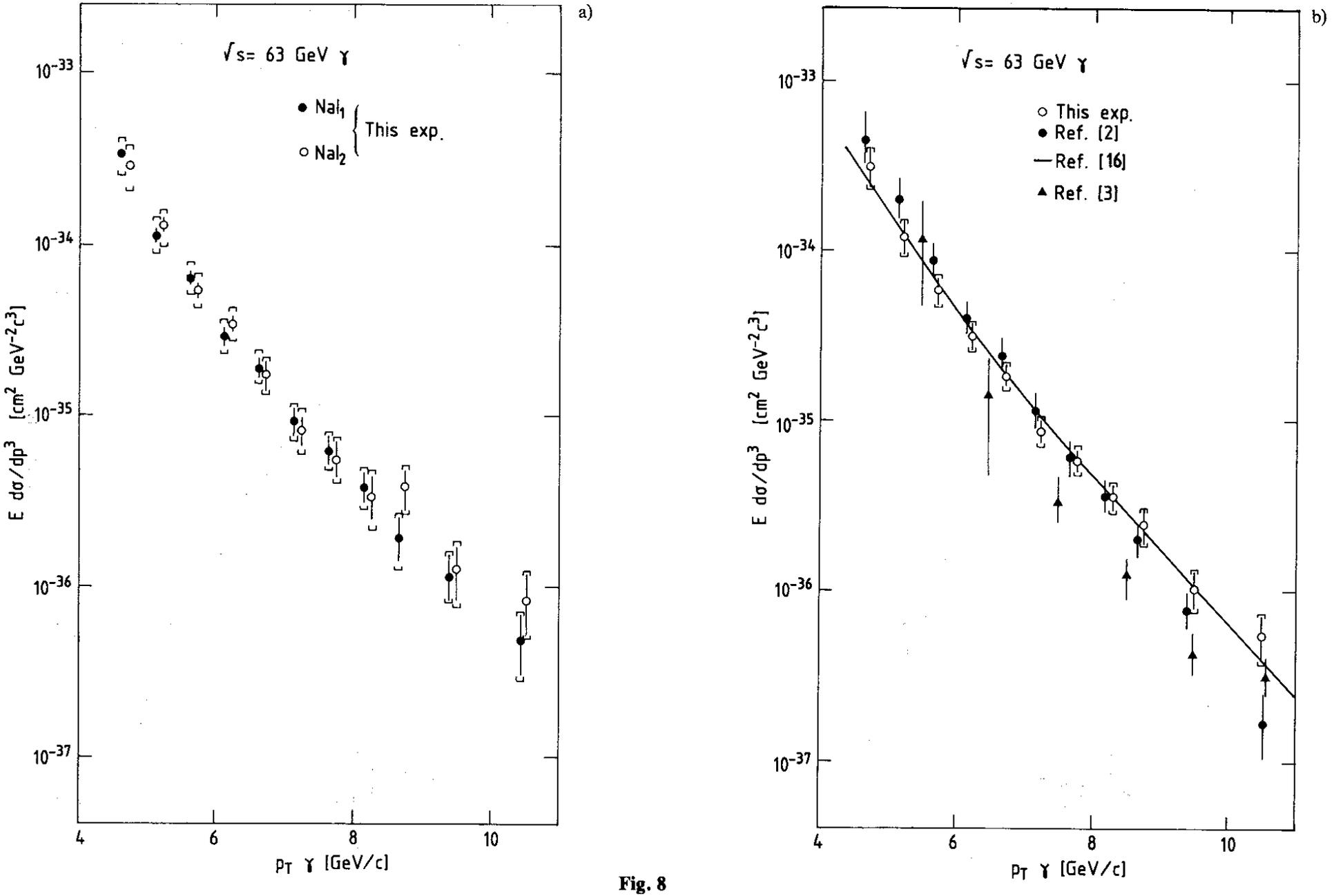
a)
√s= 63 GeV γ
● NaI1
○ NaI2
This exp.
10^-33
10^-34
10^-35
10^-36
10^-37
E dσ/dp^3 [cm^2 GeV^-2 c^3]
4
6
8
10
pT γ [GeV/c]
b)
√s= 63 GeV γ
○ This exp.
● Ref. [2]
— Ref. [16]
▲ Ref. [3]
10^-33
10^-34
10^-35
10^-36
10^-37
E dσ/dp^3 [cm^2 GeV^-2 c^3]
4
6
8
10
pT γ [GeV/c]

Fig. 8

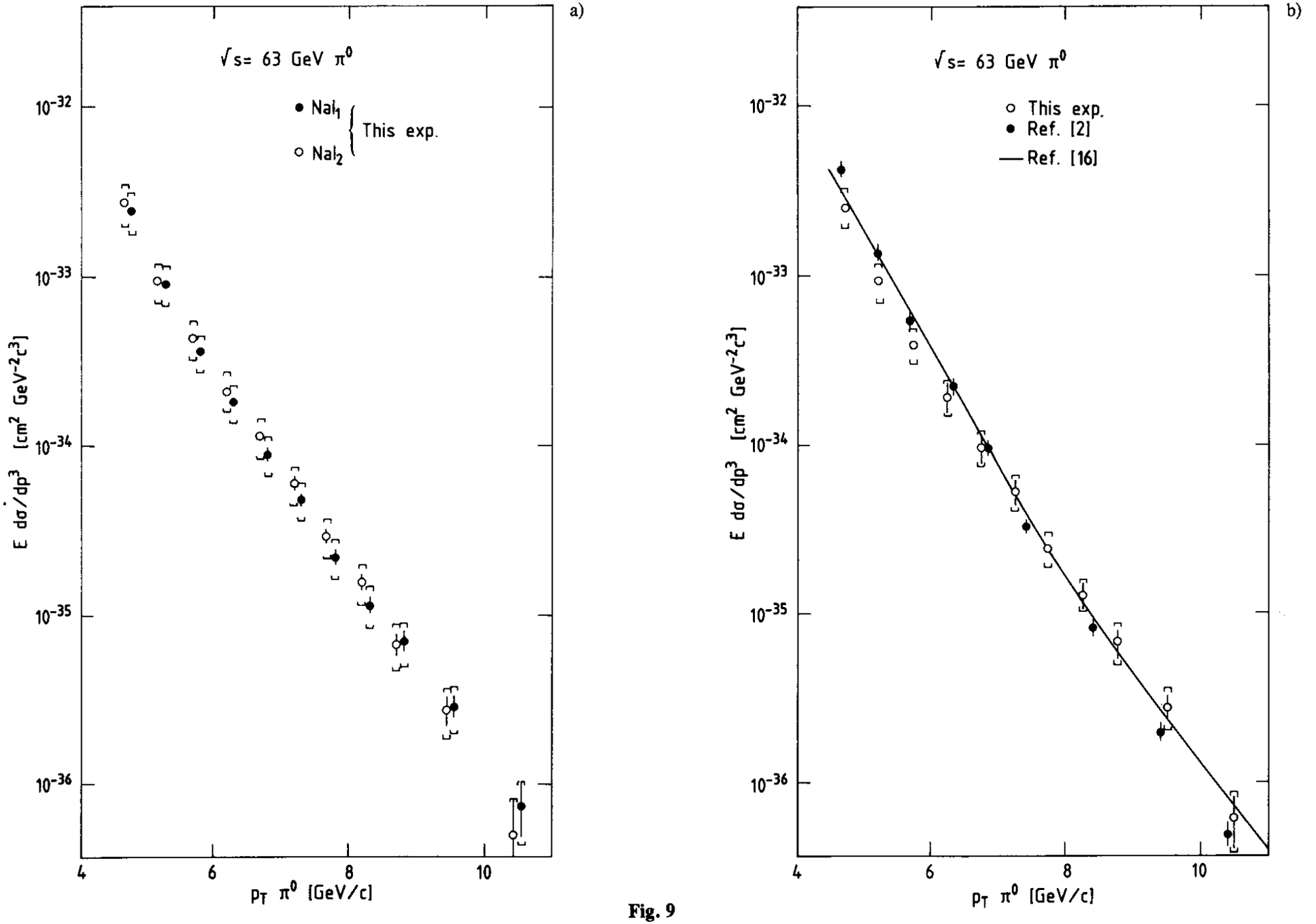
a)
√s= 63 GeV π⁰
NaI₁
NaI₂
This exp.
10⁻³²
10⁻³³
10⁻³⁴
10⁻³⁵
10⁻³⁶
E dσ/dp³ [cm² GeV⁻²c³]
4
6
8
10
p_T π⁰ [GeV/c]
b)
√s= 63 GeV π⁰
This exp.
Ref. [2]
Ref. [16]
10⁻³²
10⁻³³
10⁻³⁴
10⁻³⁵
10⁻³⁶
E dσ/dp³ [cm² GeV⁻²c³]
4
6
8
10
p_T π⁰ [GeV/c]

Fig. 9

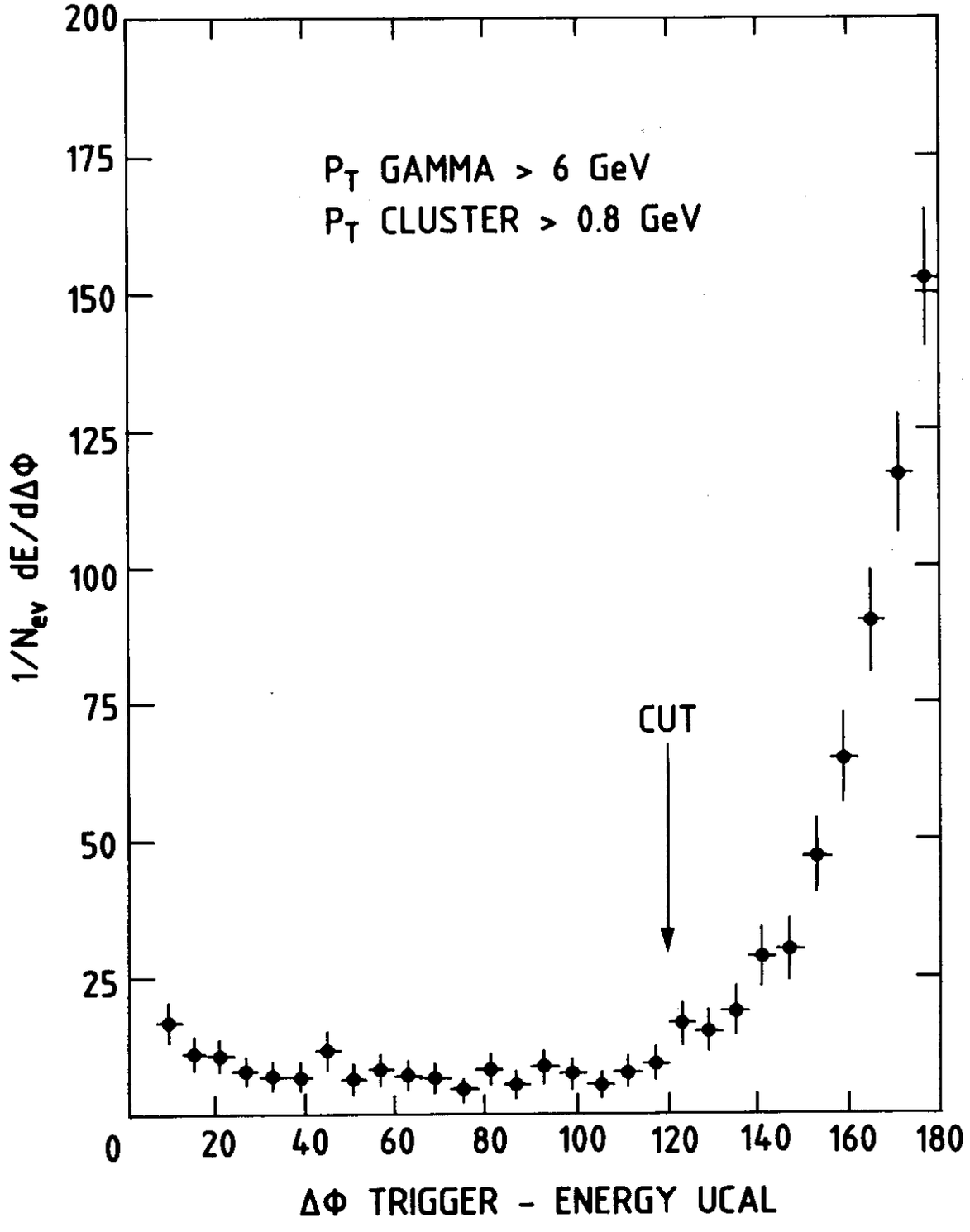
200
175
150
125
100
75
50
25
0
20
40
60
80
100
120
140
160
180
P_T GAMMA > 6 GeV
P_T CLUSTER > 0.8 GeV
CUT
$1/N_{ev}$ dE/dΔΦ
ΔΦ TRIGGER - ENERGY UCAL

Fig. 10

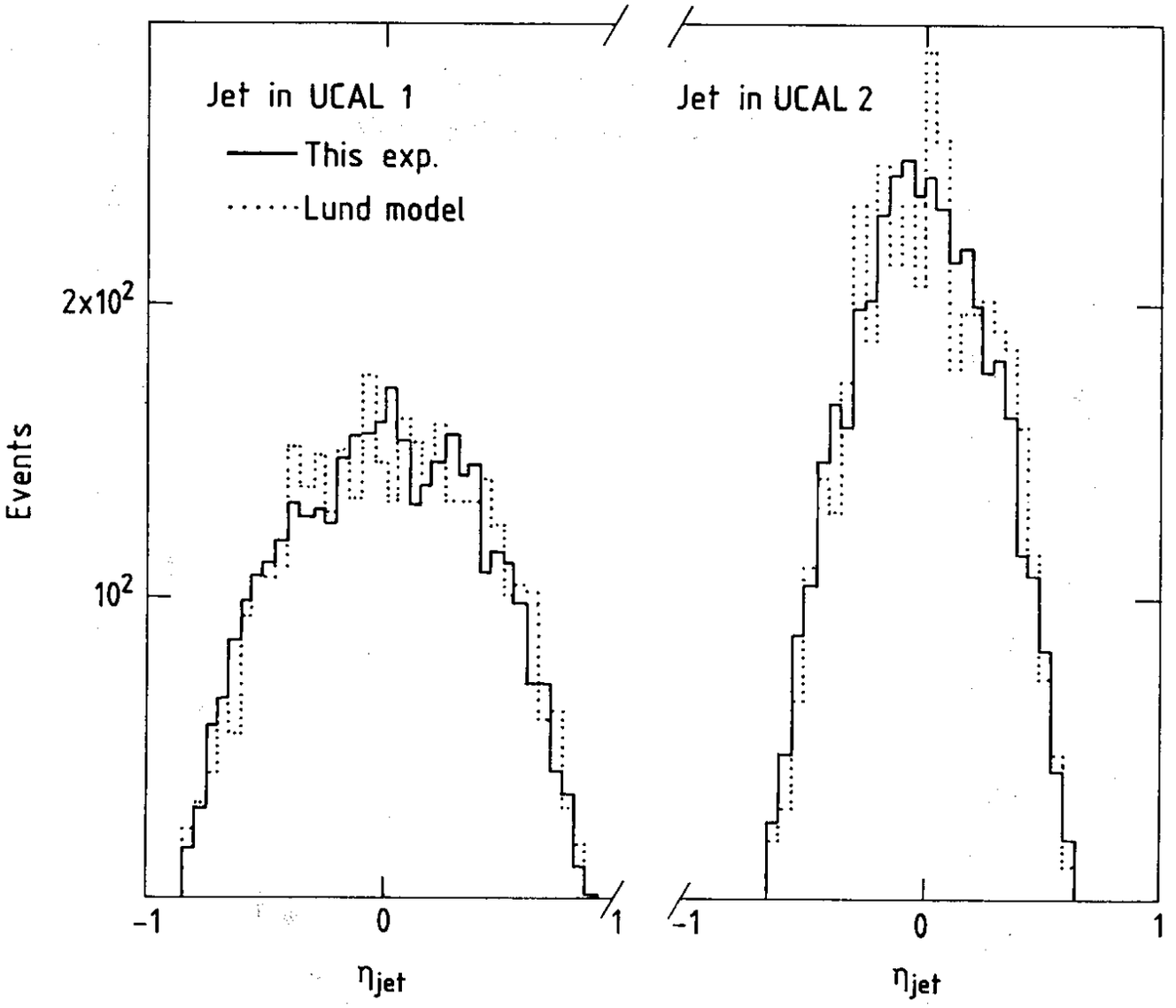
Jet in UCAL 1
This exp.
Lund model
Events
2x10²
10²
-1
0
1
ηjet
a)
Jet in UCAL 2
-1
0
1
ηjet
b)

Fig. 11

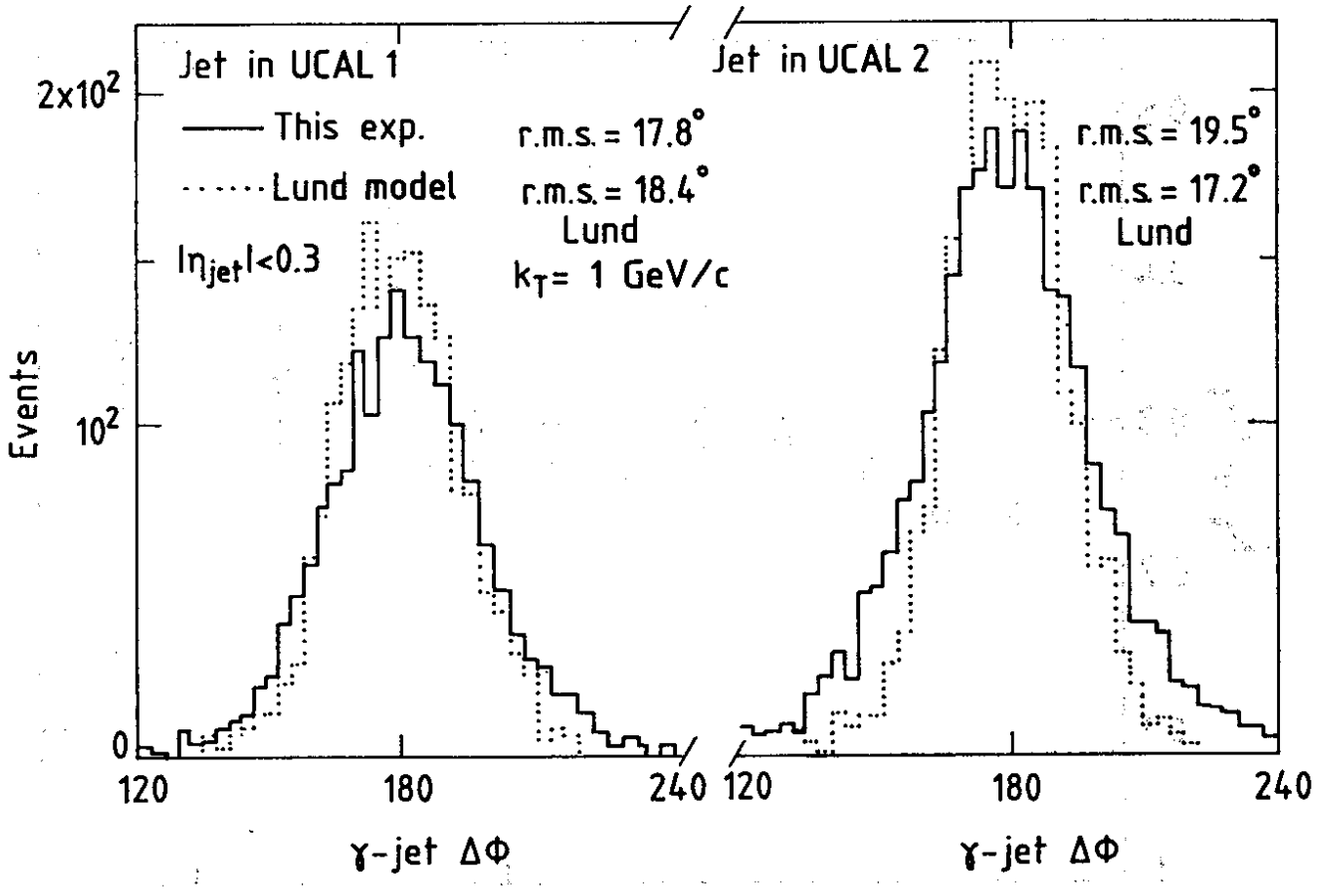
Jet in UCAL 1
This exp.
Lund model
$|\eta_{jet}|<0.3$
r.m.s. = 17.8°
r.m.s. = 18.4°
Lund
k_T = 1 GeV/c
Events
$2x10^2$
10^2
0
120
180
240
γ-jet ΔΦ
a)
Jet in UCAL 2
r.m.s. = 19.5°
r.m.s. = 17.2°
Lund
120
180
240
γ-jet ΔΦ
b)

Fig. 12

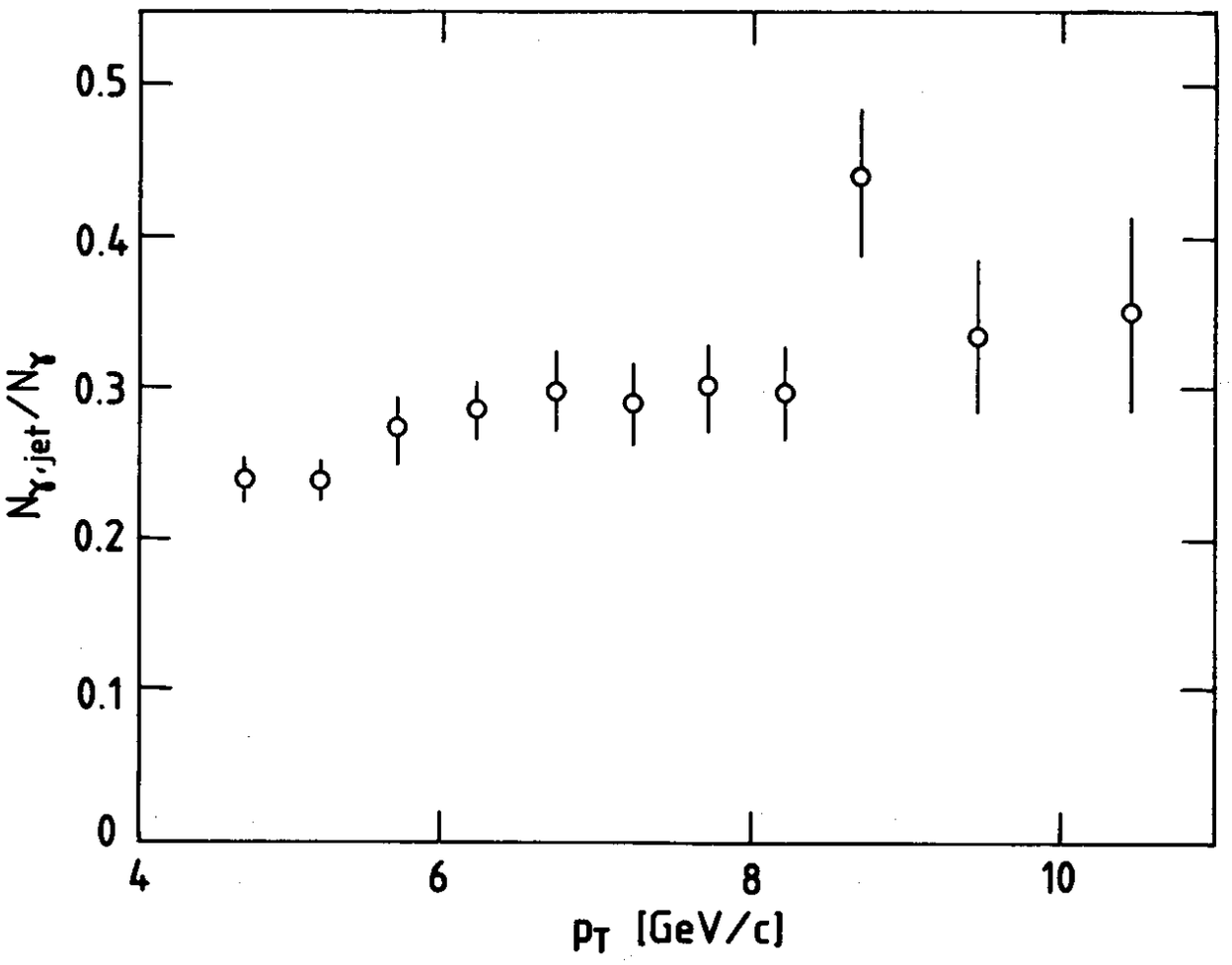

Fig. 13

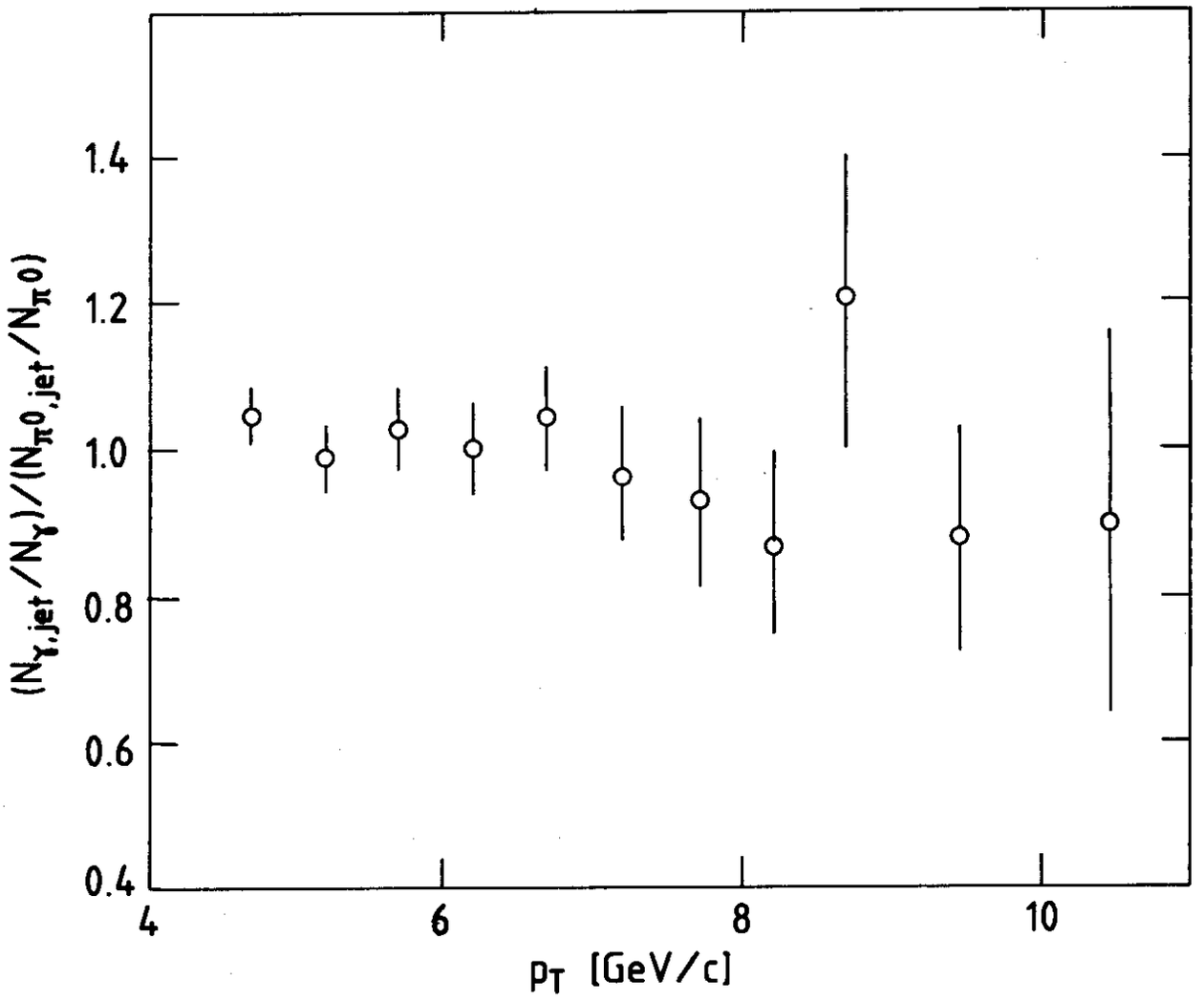

Fig. 14

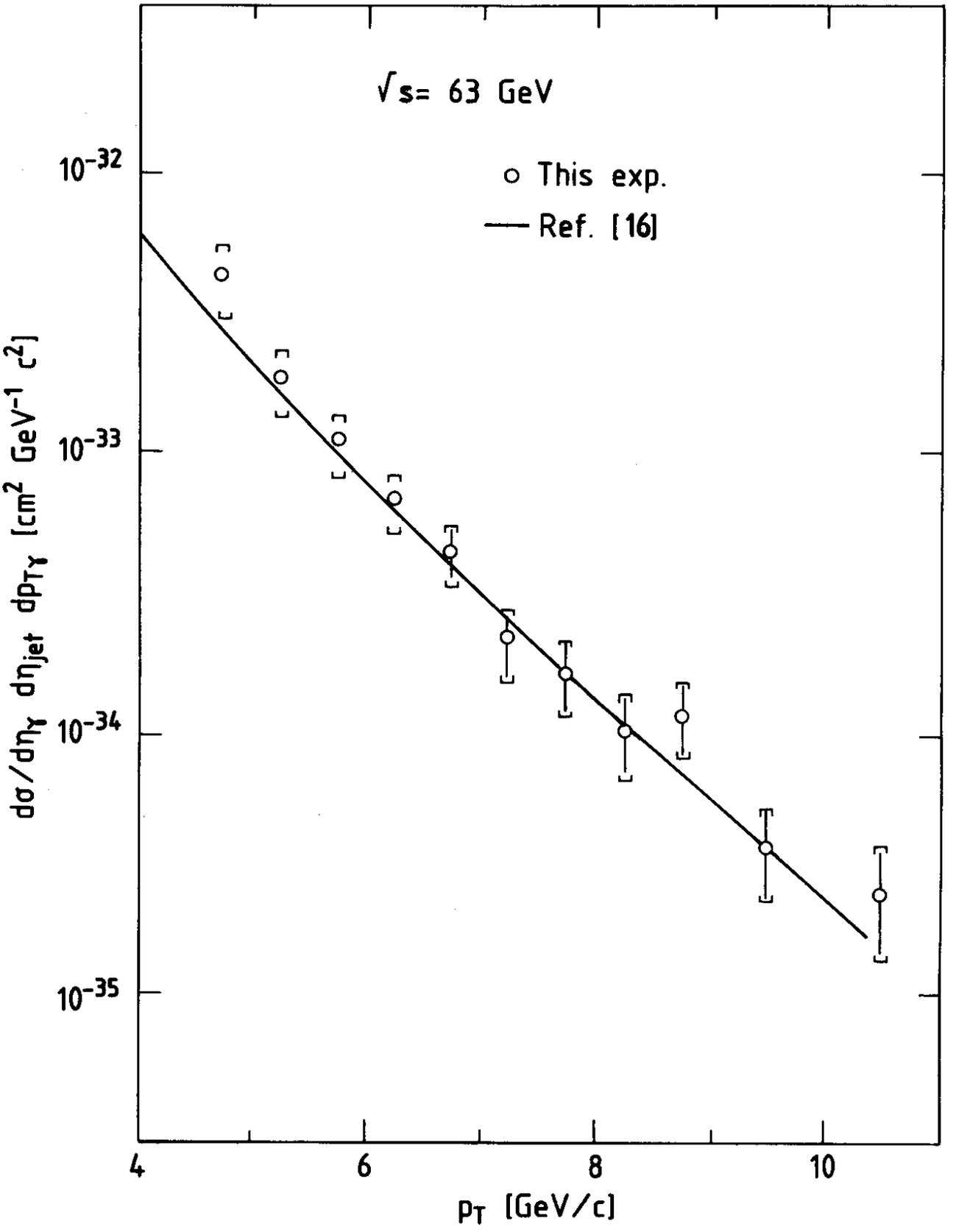
√s= 63 GeV
o This exp.
— Ref. [16]
10^-32
10^-33
10^-34
10^-35
dσ/dη_γ dη_jet dp_Tγ [cm^2 GeV^-1 c^2]
4
6
8
10
p_T [GeV/c]

Fig. 15

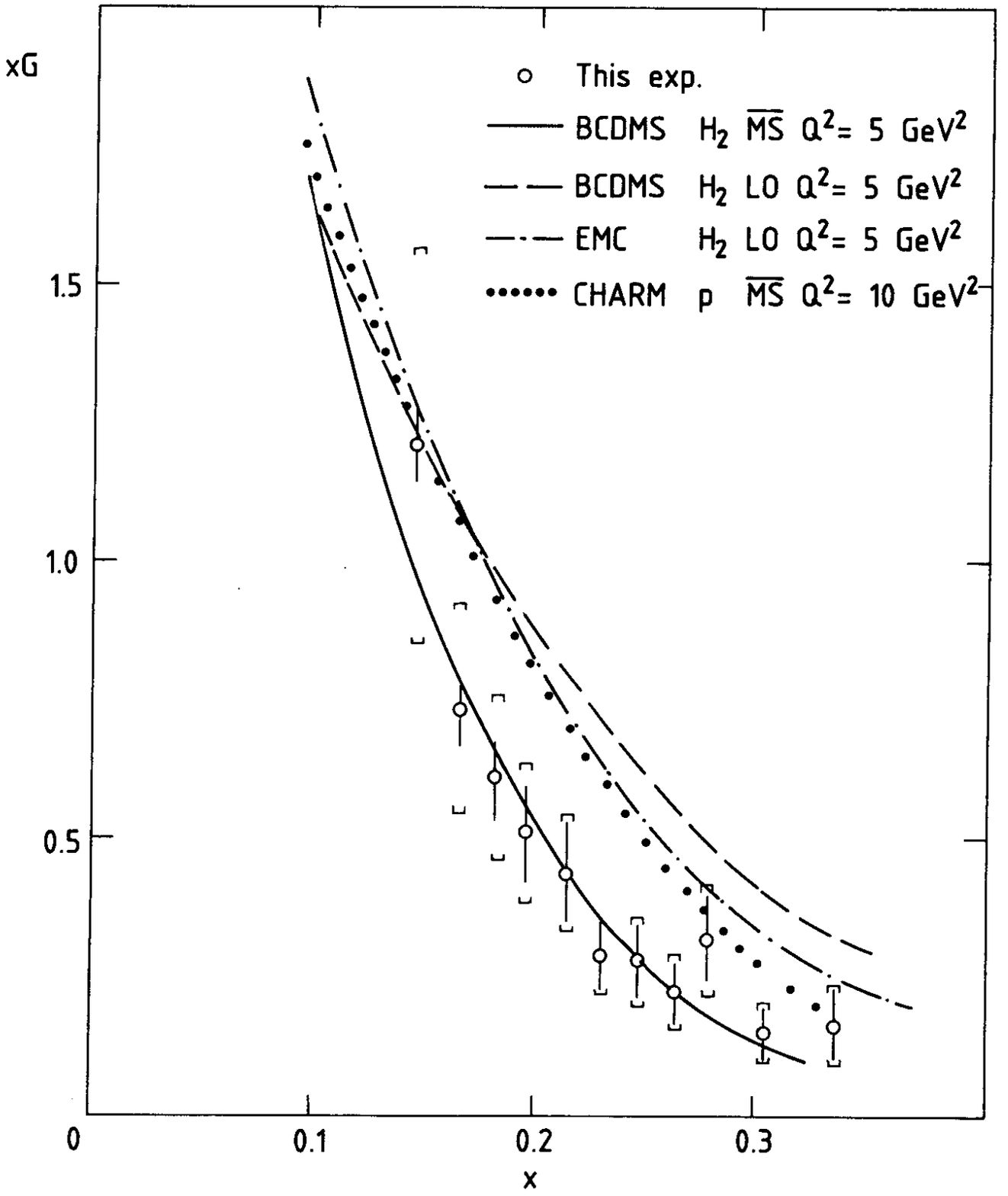
xG
This exp.
BCDMS H_2 $\overline{MS}$ Q^2= 5 GeV^2
BCDMS H_2 LO Q^2= 5 GeV^2
EMC H_2 LO Q^2= 5 GeV^2
CHARM p $\overline{MS}$ Q^2= 10 GeV^2
1.5
1.0
0.5
0
0.1
0.2
0.3
x

Fig. 16